Ultramicroscopy 25 (1988) 279–292
North-Holland, Amsterdam

CONTRAST TRANSFER FOR FROZEN-HYDRATED SPECIMENS: DETERMINATION FROM PAIRS OF DEFOCUSED IMAGES

Chikashi TOYOSHIMA *

Department of Cell Biology, Stanford University School of Medicine, Stanford, California 94305, USA

and

Nigel UNWIN

Medical Research Council Laboratory of Molecular Biology, Hills Road, Cambridge CB2 2QH, UK

Received 14 January 1988; received in revised form 30 March 1988

Electron imaging of frozen-hydrated biological molecules allows density maps to be obtained directly, without the need for fixatives or stains. The appearance of such maps may, however, be strongly influenced by the contrast transfer properties, which have not previously been evaluated by quantitative experiments. Here we determine the contribution due to amplitude contrast in a typical (~ 300 Å thick) frozen specimen, consisting of arrays of acetylcholine receptor, by comparing pairs of images recorded with different defocuses. We find that this specimen is imaged as a "weak-phase–weak-amplitude" object and that the contribution due to amplitude contrast is 7%.

1. Introduction

It is now well established that the linear theory of image formation provides a good approximation in accounting for the contrast present in electron micrographs of thin biological specimens (see ref. [1], for a recent review). In this approximation, the phase contrast produced by defocusing modulates components of the object having different spacings as $\sin \chi(\upsilon)$ (χ is the phase shift of the scattered wave and υ is the spatial frequency; see section 2) causing them to be recorded with different weights [2]. Thus there is a direct relation between the object and the image, and it is possible to compensate computationally for the variation in $\sin \chi(\upsilon)$ (i.e. the phase contrast transfer function) to derive a more accurate representation of the densities composing the specimen [3,4].

Compensation for the effect of the contrast transfer function (CTF) is not usually needed in the analysis of images of negatively stained molecules, where amplitude contrast, which modulates as $\cos \chi(\upsilon)$, largely makes up for the reduction in phase contrast that occurs at low resolution [4]. However, with unstained, ice-embedded specimens [5–7] the amplitude contrast, in the absence of heavy metal salts, has a weaker effect and compensation is more likely to be necessary [8]. In addition, specimens preserved by freezing may contain more precise information about the structure, making the accuracy of the compensation – and hence the exact proportion of the amplitude contrast – more critical. The corrections are most important with small crystalline arrays and isolated particles, where electron diffraction cannot be used to obtain a measure of the unmodulated strengths of different spatial components [9]; yet quantitative measurements of the influence of amplitude contrast in such cases have not so far been made.

* Present address: Medical Research Council Laboratory of Molecular Biology, Hills Road, Cambridge CB2 2QH, UK.

In this paper, we examine the behaviour of the CTF for thin ice-embedded specimens within the framework of the linear theory of image formation, using as a test object acetylcholine receptor enriched membranes from the electric ray *Torpedo marmorata*. These membranes form tubular arrays which can be treated as superimposed two-dimensional crystals when flattened down onto support films [10]. The unit cell has dimensions of 90 Å × 162 Å, an included angle of 120° and p2 symmetry. The length of the receptor molecule is about 140 Å [11]. The crystals diffract to about 20 Å resolution. Thus, the specimen is typical of many molecular assemblies studied by electron microscopy. From analysis of pairs of images recorded at different defocuses, we find that it is imaged as a "weak-phase–weak-amplitude" object and that the contribution made by amplitude contrast is 7%.

2. Methods

2.1. Electron microscopy

Preparation of the crystalline acetylcholine receptor tubes from *Torpedo marmorata* was as described [12]. Five μl aliquots of solutions containing the tubes were applied to carbon films glow-discharged in amylamine vapour and supported by 400-mesh copper grids. Excess solution was blotted off and the grid was plunged into liquid ethane slush to embed the specimens in amorphous ice.

Electron micrographs were recorded at 120 kV with a Philips EM400T equipped with an auxiliary anticontamination device. A 50 μm (nominal diameter) objective aperture was always in place. A 50 μm condenser aperture was used with a first condenser setting of 4. The grids were mounted under liquid nitrogen in a prototype Gatan Mark 2 cryo-holder, and the temperature of the specimen kept at −167°C; the stability of the holder was sufficient to provide better than 10 Å resolution. The objective lens current was continuously monitored and made constant (6.20 ± 0.02 A) by adjusting the specimen height prior to photography. Grids were scanned at 2800 × and the focus was adjusted at 170000 × on an area adjacent to the one of interest; images were recorded on Kodak S0163 film at a calibrated magnification of 34900 × using a low-dose kit. Illumination conditions were chosen so that an optical density of one was produced with a one-second exposure when films were developed for 12 min in Kodak D19 developer. Three to five micrographs were recorded of each field, using different defocuses; the last micrograph was recorded at the same defocus as the first to assess radiation damage. The difference in focus between consecutive pictures was usually about 8000 Å or 16000 Å; underfocus–overfocus pairs were taken at about ±12000 Å or ±22000 Å defocus (the positive values corresponding to underfocus).

Electron dose was estimated from the optical density of the film exposed to 100 kV electrons, assuming an electron speed of 2.2. The dose used to record one image was 6 to 8 electrons/Å^2.

2.2. Analysis of the tube images

Electron micrographs were screened initially by optical diffraction and the good images were digitised on a Perkin-Elmer flatbed microdensitometer, using a sampling distance and aperture size of 15 μm and 16.6 μm, respectively. Each image of a tube consisted typically of 1200 × 200 pixels (~ 5000 × 1000 Å), and was padded to a 1536 × 512 array size, from which Fourier transforms were calculated using a VAX-11/785 or VAX-8550 computer. The optical densities from each image were normalised so that the standard deviation of the value in a region adjacent to the tube was the same as that of the first picture in the series. Since the stability of the microdensitometer was reasonably good, this method gave scaling factors practically identical to those determined from the mean of the optical densities.

After determining the unit cell vectors, amplitudes of strong reflections were extracted from the transform [13]. To make the comparisons accurate, all images in a series were rotationally aligned by quadratic interpolation relative to the first image, so that the unit cell vectors all pointed in the same direction with respect to the sampling raster. Integrated amplitudes were used in assign-

ing strengths to the individual reflections. The integration was done using the square of the amplitude, which is fairly insensitive to the area used in the summation since the sum is dominated by the points with high amplitudes. However, the integrated amplitude is sensitive to the shape of the peak, which seemed to be the most serious source of error. Consequently, if the profile of the spot was apparently different within a pair of images being compared, that reflection was discarded. Only quality 1 spots (amplitude higher than background by at least 7 times [14]) were used with images defocused by more than 10000 Å. For images defocused by less than this amount, the signal-to-noise ratio was poorer and even well defined spots failed to attain a quality of 1; thus if diffraction from the two sides of the tube gave similar values, quality 2 spots were also used, but in this case they were averaged.

The thickness of the ice surrounding some of the tubes was estimated from the micrographs as described by Eusemann et al. [15], assuming a semi-angle for the objective aperture of 15 mrad, as calibrated with diffraction patterns from thin gold films. The estimates involved measurement of the optical densities over a hole, next to the tube (i.e. ice plus carbon) and over an adjacent area of the carbon film from which the ice had been removed by sublimation.

2.3. Evaluation of the CTF

At least three components may contribute to image formation of thin biological specimens, namely phase, amplitude and aperture (or scattering) contrast. Phase contrast is related directly to the potential field of the specimen and arises from interference of the unscattered and elastically scattered waves, after distortion of the wavefront in the diffraction plane of the objective lens. Amplitude contrast may arise from attenuation of the coherent incident wave by, for example, inelastic scattering and can be incorporated in the theory by introducing a complex potential [16]. Aperture contrast (which arises from electrons scattered outside the objective aperture) has also sometimes been included as an additional attenuation of the elastic wave (e.g., refs. [16–18]). Thus the object wave function contains both real and imaginary terms. These are modified in the diffraction plane by the phase shift, χ, due to spherical aberration and defocusing:

$$\chi = 2\pi\lambda^{-1}\left(\tfrac{1}{2}\,\delta f\,\theta^2 - \tfrac{1}{4}C_s\theta^4\right)$$

(where δf is the degree of underfocus, C_s is the spherical aberration coefficient, λ is the electron wavelength and θ is the scattering angle), and this phase shift modulates the contrast in the image.

The modulations in contrast due to the electron-optical parameters are most simply expressed in the Fourier transform, or diffraction pattern, of the image of an amorphous object, where they are manifested as a set of rings of intensity concentric about the origin (Thon rings [19], see fig. 2). The positions of these rings reflect the contributions made by the real and imaginary terms of the

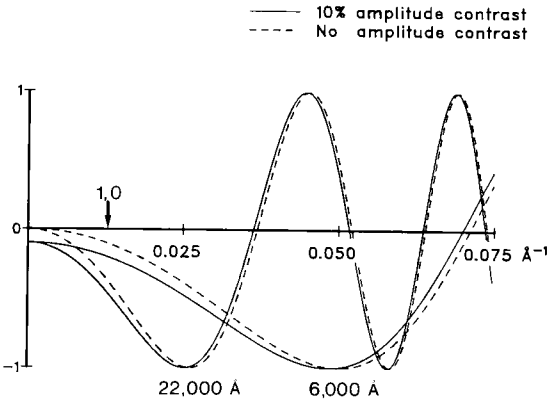

Fig. 1. Theoretical CTFs, $C(v)$, for 6000 Å and 22000 Å underfocus, assuming pure phase contrast (broken lines) or 10% amplitude contrast (solid lines). By comparing the ratio of the CTFs at a given spatial frequency, it is possible to estimate the proportion of amplitude contrast. For example, at a spatial frequency of 0.025 $Å^{-1}$ (40 Å resolution, corresponding to the (1,2) or (1,−4) reflections), the two curves give quite different values (−0.383 and −0.474) when the underfocus is 6,000 Å, but almost identical values when the underfocus is 22000 Å; thus the ratio of the values for the two defocuses is determined by the proportion of amplitude contrast. The ratios provide an even more sensitive measure of the proportion of amplitude contrast in the lower spatial frequency region, e.g. at a resolution corresponding to that of (1,0) reflection (marked). See also table 1.

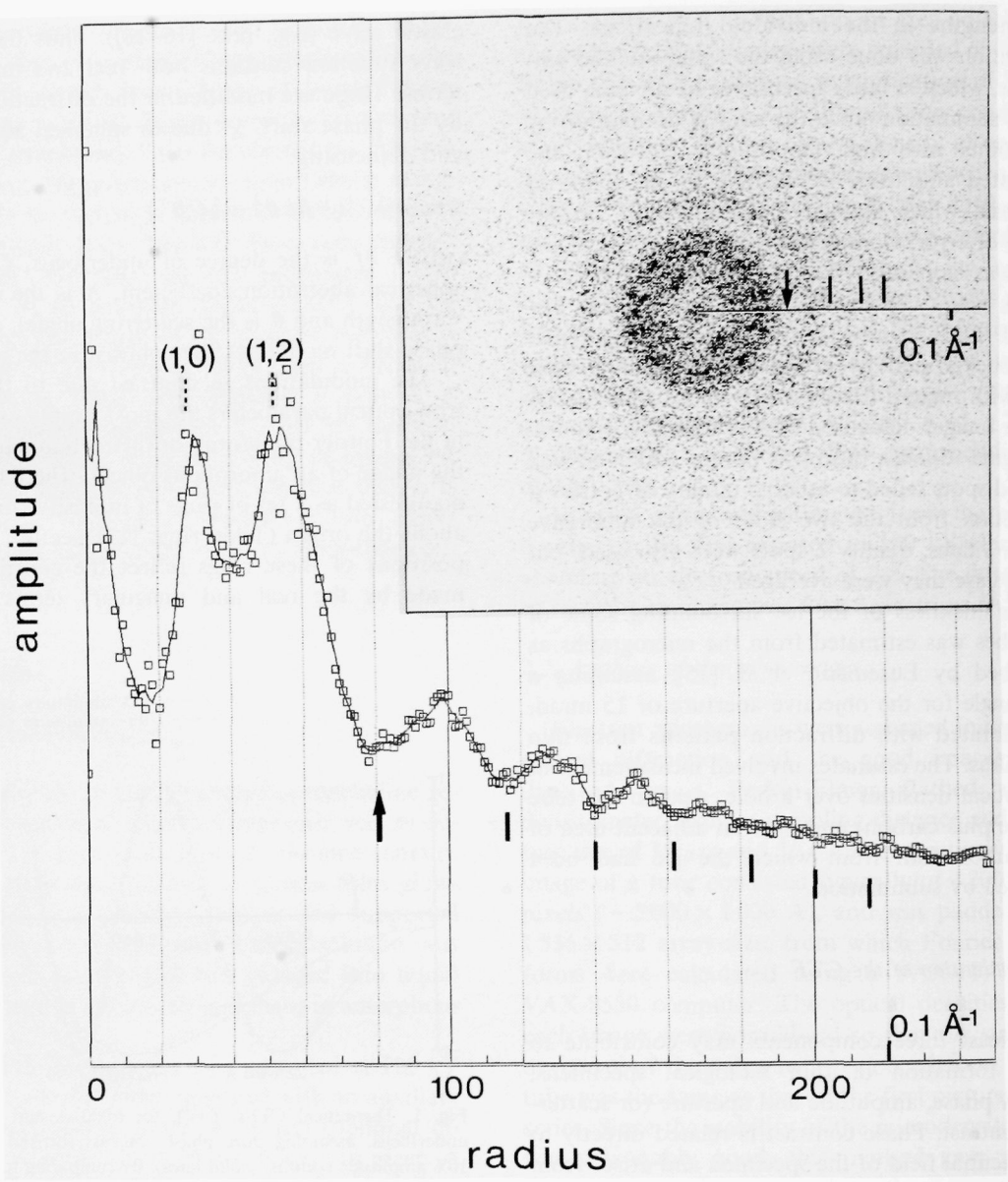

Fig. 2. Mean radial amplitude distribution of the Fourier transform of the image in fig. 4b (22000 Å underfocus), used to determine the location of first minimum of the Thon rings. The locations of the first- (arrow) and higher-order minima (vertical bars) and the (1,0) and (1,2) reflections are marked. The abscissa is in grid units (1 grid unit = 0.000454 $Å^{-1}$). The solid line represents a running average over 5 points. The inset shows the corresponding computed Fourier transform, with positions of the minima marked. Note that the strong peaks and troughs in the radial plot at low resolution (less than 80 grid units) arise from the strong reflections, whereas the ripples at higher resolution correspond to the Thon rings.

object wave function in creating the image. The total contribution can be written:

$$C(\upsilon) = A(\upsilon) \sin \chi(\upsilon) + B(\upsilon) \cos \chi(\upsilon),$$

where A and B represent the fractional contributions due to the phase and amplitude contrast transfer functions respectively, and $\upsilon(=\theta/\lambda)$ is

the spatial frequency, or reciprocal of the spacing in the object. In this paper we refer to $C(v)$, which combines both phase and amplitude terms, as the CTF (although strictly speaking the CTF is a specimen-independent term).

The amplitude contrast contribution, B, can be determined by comparing the amplitudes of reflections in Fourier transforms of two images of the same specimen recorded at different defocuses (see fig. 1). If the exact values for the two defocuses were known the determination would be straightforward. However, these values are not evident directly from the locations of the Thon rings, which depend on both the defocus and the amount of amplitude contrast. Therefore we calculated the ratio of the amplitudes of a particular reflection at two defocuses as a function of the locations of the first minimum in the Thon rings, assuming different amounts of amplitude contrast. By measuring the locations of the first minimum and matching the experimental data with the calculations, the actual proportion of amplitude contrast could be readily established. Test calculations showed that the accuracy of this method is not sensitive to differences in amplitude contrast at the spatial frequency corresponding to the first minimum and at the spatial frequency being examined, provided that the proportion of the amplitude contrast (B) is much smaller than the phase contrast (A), as is the case here.

To measure the positions of the first minimum, the images of the tubes, consisting typically of 512×220 pixels, were expanded to a 512×512 array size and Fourier-transformed (fig. 2, inset). One half of each Fourier transform was divided into five equal sectors, and for each sector the mean amplitude values at different radii were calculated and plotted. If these sector-averages were judged to be consistent (i.e. no obvious astigmatism, drift etc.), they were averaged further to provide an overall amplitude profile (fig. 2); otherwise, the image was considered unsuitable for analysis and rejected. The location of the first minimum was obtained directly from the overall amplitude profile, or (where possible) by fitting the zeros in theoretical CTFs to the set of higher-order minima that usually were also present.

3. Results

The experimental conditions were chosen so that the locations of the Thon rings and the amplitudes of the reflections could both be measured accurately from the same area of specimen. This necessitated an electron dose sufficiently high

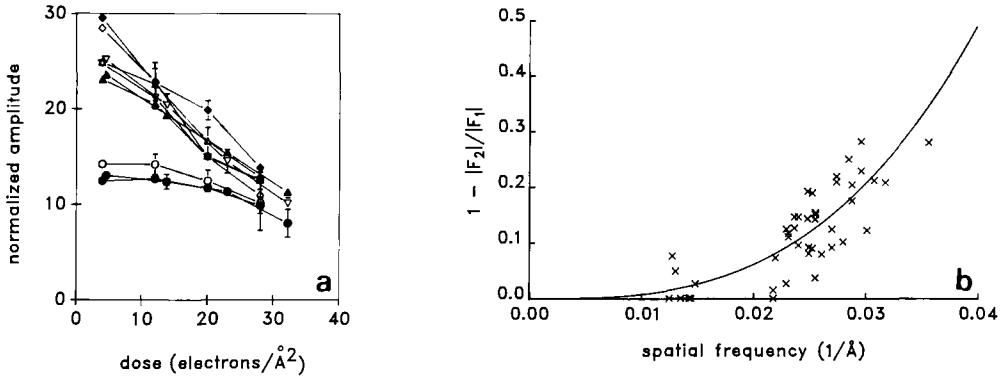

Fig. 3. Radiation damage of the acetylcholine receptor tube in ice. (a) Amplitudes of several strong reflections plotted as a function of electron dose. The amplitude of each reflection has been normalized according to its spatial frequency to show that the fall-off depends primarily on the spatial frequency; the length of the error bars indicates the difference between the amplitudes from two sides of the tube. Filled circles, (1,0); open circles, (0,2); solid triangles, (1,2); open triangles, (2,0); inverted triangles (1,−4); open diamonds, (0,4); solid diamonds, (1,3). (b) Fractional decrease of amplitude of reflections in the transform of the second image, $|F_2|$, with respect to those of the first $|F_1|$, plotted as a function of their spatial frequency. The solid line shows a regression curve used for correction of radiation damage in the subsequent analyses.

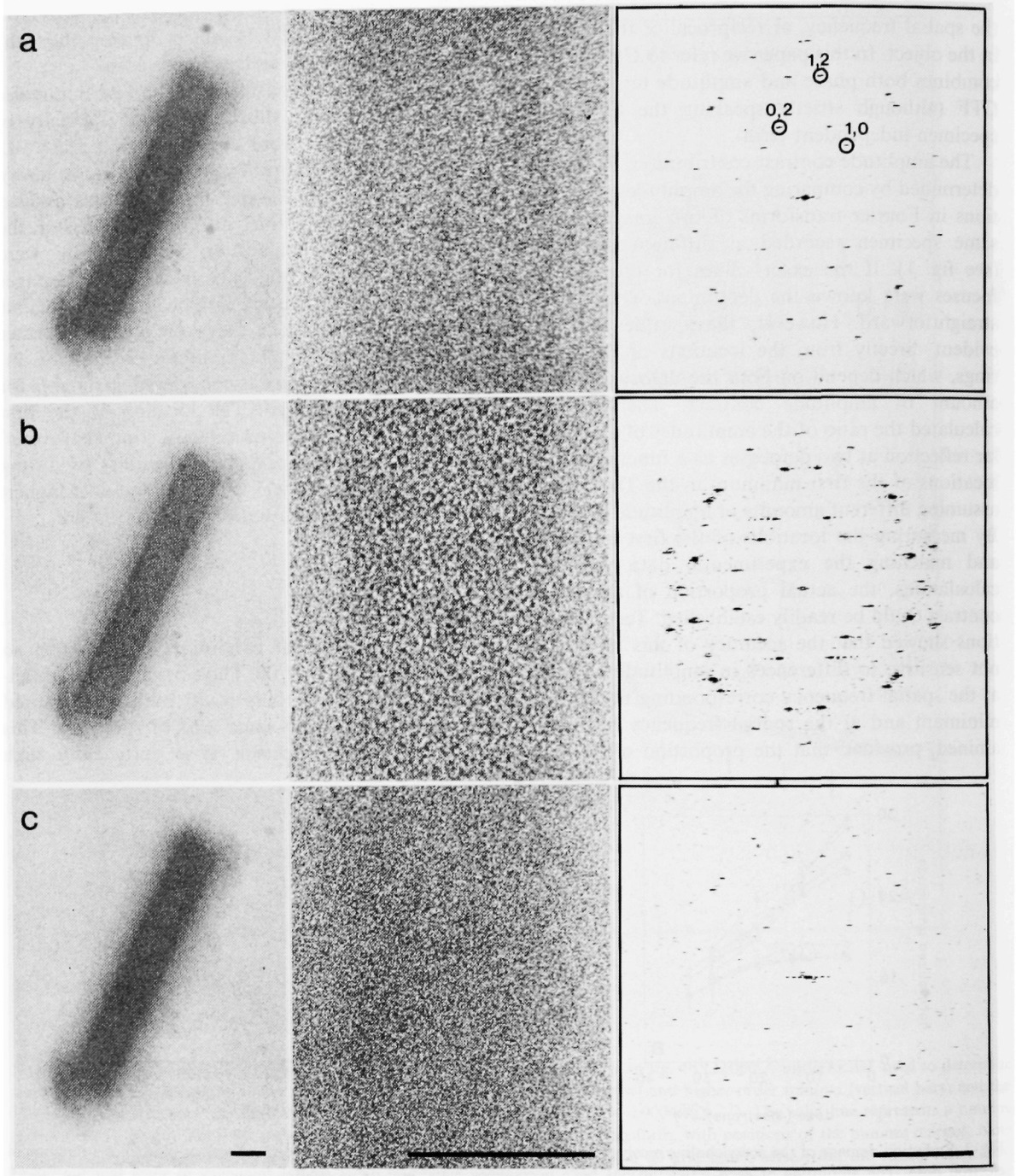

Fig. 4. A set of images (left-hand column, general view; middle, enlarged view) of a tube embedded in thin amorphous ice over a thin carbon film and their computed Fourier transforms (right-hand column). The first two images were recorded at different underfocus values (5700 Å in (a) and 22000 Å in (b)) to determine the amplitude contrast contribution, and the third (same underfocus as the first) was recorded for evaluating the effect of electron irradiation. Several strong reflections from one side of the tube are indexed. The (1,0) has a reciprocal spacing of $\sim 1/80$ Å^{-1}. Note that it is difficult to see evidence for crystallinity in the images at small underfocus ((a), (c)), yet the diffraction patterns clearly indicate its presence; the diffraction pattern from the third image, (c), has a poorer signal-to-noise ratio than the first two because of radiation damage. These images relate to the theoretical curves in fig. 1. Bars correspond to 0.1 μm (left and middle) and $1/50$ Å^{-1} (right).

(5–10 electrons/Å^{-2}) that the influence of radiation damage could not be neglected. Hence our first step was to examine the radiation sensitivity of the specimen.

3.1. Radiation damage

Several series of micrographs were recorded at identical defocuses and with insignificant irradiation between exposures, so that the amplitudes of individual reflections could be determined as a function of the total electron dose. Results (fig. 3a) showed that the higher resolution reflections (at ~ 1/40 Å^{-1}) decayed to about half of their original value after a dose of only ~ 30 electrons/Å^2, whereas the lower resolution reflections (at ~ 1/80 Å^{-1}) were relatively stable. Thus the decay rate depended primarily on the spatial frequency.

The decrease in amplitude of each major reflection in the second image, relative to the first, was plotted against spatial frequency (fig. 3b). A regression curve was fitted to the experimental points and used in the analyses of image pairs (see below) to provide an approximate correction for the radiation damage.

3.2. Determination of amplitude contrast

3.2.1. Experiments with pairs of underfocused images

Typically, sets of three micrographs were recorded from each of the tubes, selecting only those specimens embedded in thin ice (see fig. 4). The first two micrographs of the set were recorded at different, preselected levels of underfocus and used for the estimates of amplitude contrast, while the last of the set (at the same defocus as the first) was used to provide a check on the amount of radiation damage. Most often the first micrograph was recorded at the smaller defocus; however in several of the sets, the first micrograph was recorded at the higher defocus to minimise errors in correcting for radiation damage.

If the linear theory outlined in Methods were invalid, the amplitude contrast would not necessarily contribute as a cosine term and could have a defocus dependence. Therefore its contribution was determined first of all using the smallest realistic defocus difference. Given the limited accuracy of the amplitudes of the reflections obtainable in the Fourier transforms of a small tubular crystal a figure of 8000 Å was considered an appropriate defocus difference, and most experiments were carried out with underfocus pairs (~ 7000 Å and ~ 15000 Å) providing the best enhancement of the spacings of interest. In these pairs, the three low resolution reflections at about 1/80 Å^{-1}, namely the (1,0), (1, − 2) and (0,2), produced the most reliable amplitude ratios; higher resolution reflections, such as the (1,2), (2, − 2) and (1, − 4), were less reliable, being more affected by the corrections for radiation damage and less sensitive to the amount of amplitude contrast (see table 1). The experimental points for most reflections were found to lie between 5% and 10% amplitude contrast (fig. 5; circles), and although

Table 1
Theoretical ratio of amplitudes of reflections for different amounts of amplitude contrast [a]

Spatial frequency	1/80 Å^{-1}			1/40 Å^{-1}		
Amplitude contrast	0%	5%	10%	0%	5%	10%
Defocus pairs (Å)						
7000/15000 [b]	0.470	0.562	0.628	0.532	0.567	0.600
6000/22000 [b]	0.278	0.370	0.443	0.387	0.431	0.474
±12000 [b]	−1.000	−0.960	−0.331	−1.001	−0.906	−0.820
±22000 [b]	−1.000	−0.766	−0.580	−1.000	−0.988	−0.875
±22000 [c]	−1.000	−0.752	−0.559	−1.000	−0.904	−0.817

[a] Smaller defocus divided by larger defocus.
[b] Assuming amplitude contrast to be a cosine term.
[c] Assuming amplitude contrast to be a constant term.

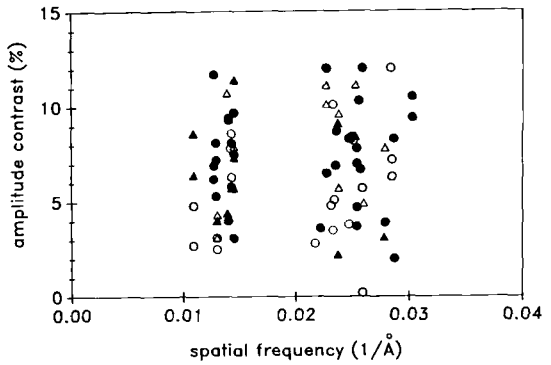

Fig. 5. Proportion of amplitude contrast determined by comparing two underfocused images, as a function of spatial frequency. The focus difference between the two image pairs was about 8000 Å (circles) or 16000 Å (triangles). Filled and open symbols indicate that the first image was taken at a smaller (filled symbols) or a larger (open symbols) defocus value than the second. The two recording sequences were adopted to minimize errors arising from the correction of radiation damage.

higher resolution reflections gave more scatter, there was no obvious dependence on spatial frequency.

Additional experiments were conducted using larger defocus differences (16000 Å) to examine the defocus dependence, if any, of the amplitude contrast. The amplitude ratios of the reflections are more strongly dependent on the amplitude contrast at the larger defocus differences (see table 1) and, in principle, a more accurate determination of the amplitude contrast is possible under these conditions. As shown in fig. 5 (triangles) there is no detectable dependence of the amplitude contrast on the defocus over the range of spatial frequencies evaluated.

The average amplitude contrast contributions for the reflections at $\sim 1/80$ Å^{-1} and $\sim 1/40$ Å^{-1} were 6.6% (SD = 2.5%, $n = 33$) and 7.0% (SD = 3.0%, $n = 43$), respectively.

3.2.2. *Experiments with pairs of underfocused–overfocused images*

If the linear theory is valid, the most sensitive method to measure the amount of amplitude contrast, at least at low resolution, should be to compare underfocused–overfocused pairs of images recorded at small defocuses (see table 1; fig. 6). This is because phase contrast and amplitude contrast contribute with opposite sign and tend to cancel when the image is overfocused, but contribute with the same sign and add when the image is underfocused. Diffraction patterns of underfocused–overfocused pairs of images clearly illustrate this effect. An example for ±12000 Å defocus is given in fig. 7. It can be seen that the lower resolution reflections in the diffraction pattern (fig. 7c) from the overfocused image (fig. 7b) are much weaker, due to partial cancellation, than those from the underfocused image (fig. 7a). Quantitative results obtained from ±12000 Å pairs of images (fig. 8) gave essentially the same values for the amplitude contrast as were obtained from the underfocused pairs (fig. 5): the average amplitude contrast contributions for the reflections at $\sim 1/80$ Å^{-1} and $\sim 1/40$ Å^{-1} were 6.7% (SD = 2.0%, $n = 31$) and 6.8% (SD = 3.2%, $n = 37$), respectively. Consistent with the increase in sensitivity, scatter associated with the lower resolution reflections is smaller in fig. 8 than in fig. 5.

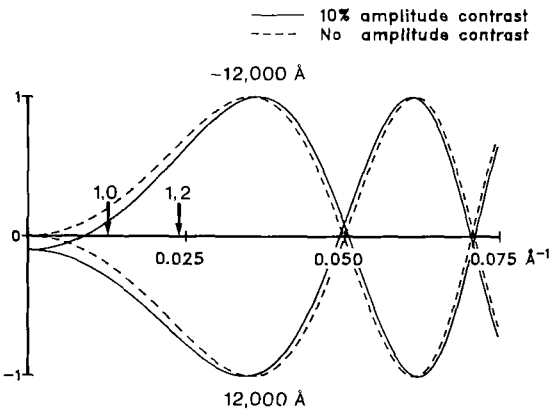

Fig. 6. Theoretical CTFs for the defocus conditions realized in fig. 7 (±12000 Å defocus). Solid and broken lines correspond to 10% and 0% amplitude contrast, respectively. The spatial frequencies corresponding to the (1,0) and (1,2) reflections are indicated; at these low spatial frequencies the phase and amplitude contrast contributions are of opposite sign and therefore tend to cancel when the image is overfocused, but are of the same sign and reinforce one another when the image is underfocused. Thus at low spatial frequencies comparison of underfocused–overfocused pairs of images provides a sensitive means of measuring the amplitude contrast contribution.

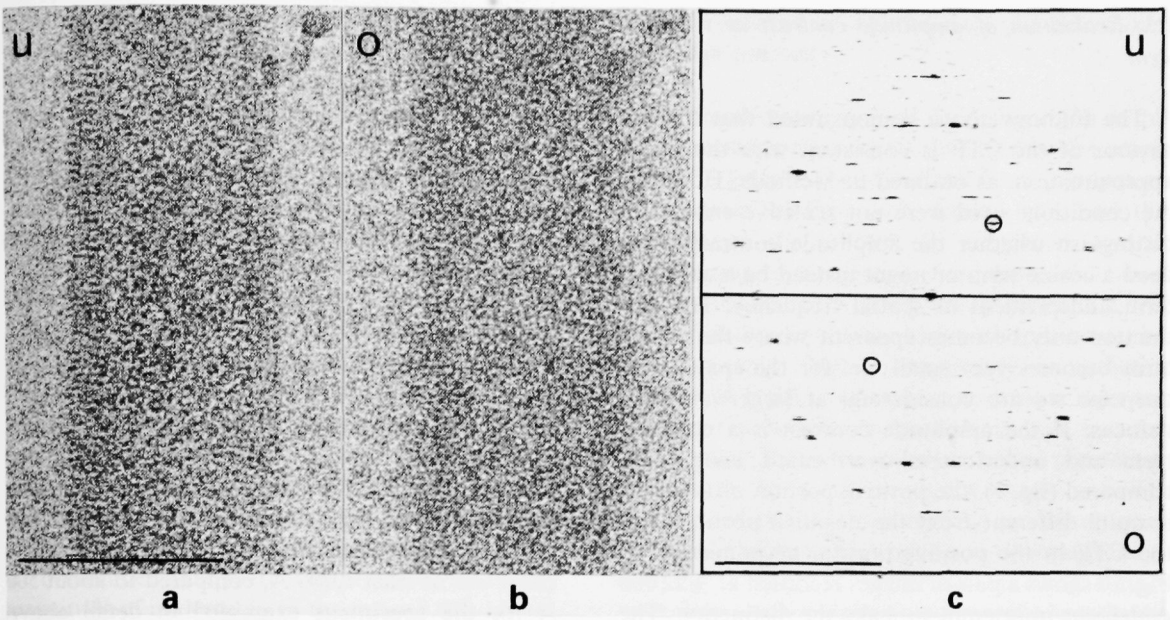

Fig. 7. Images of an ice-embedded tube recorded at 12000 Å underfocus (a) and 12000 Å overfocus (b), and a composite of their diffraction patterns (c). The (1,0) reflections from one side of the tube are marked. U and O denote under- and overfocus, respectively. Note that lower resolution reflections appear much weaker in the diffraction pattern from the overfocused image (lower half, (c)) than in the underfocused one (upper half, (c)), due to a partial cancellation of phase and amplitude contrast. The overfocused image was recorded after the underfocused image so that the effect cannot be due to radiation damage. Bars correspond to 0.1 μm (a) and 1/50 Å^{-1} (b).

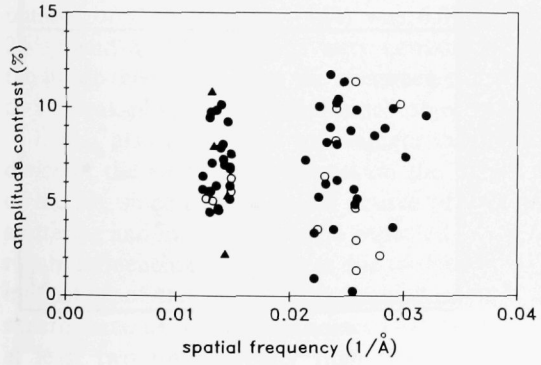

Fig. 8. Proportion of amplitude contrast determined by comparing underfocused–overfocused pairs of images, as a function of spatial frequency. Images were taken at about ±12000 Å (circles) or ±22000 Å (triangles) defocus. Filled symbols indicate that the first image was underfocused; open symbols indicate that the first image was overfocused.

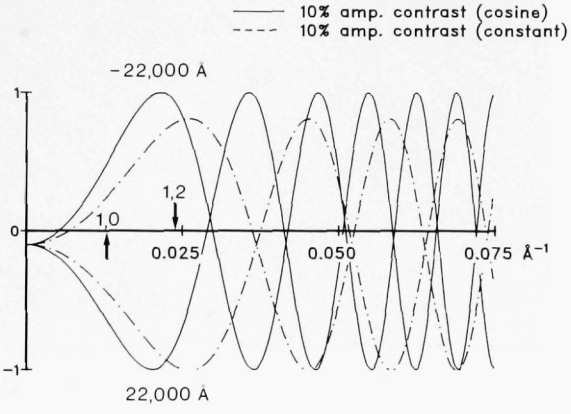

Fig. 9. Theoretical CTFs for ±22000 Å defocus. The solid line corresponds to the case where amplitude contrast is described by a cosine term ("weak-phase–weak-amplitude" object) and dash-dotted line to the case where amplitude contrast is a constant term. The spatial frequencies corresponding to the (1,0) and (1,2) reflections are indicated.

3.3. Evaluation of amplitude contrast as a cosine term

The findings above demonstrated that the behaviour of the CTF is consistent with the linear approximation, as outlined in Methods. However, the conditions used were not sensitive enough to distinguish whether the amplitude contrast is indeed a cosine term or might instead be a constant term, independent of spatial frequency. The distinction only becomes apparent where the cosine term becomes very small, i.e. for the spatial frequencies we are considering, at large values of defocus. If the amplitude contrast is a constant term and underfocused-overfocused images are compared (fig. 9), the positive portion of the CTF is quite different from the negative portion, and the CTF in the positive portion never reaches 1. Fig. 10 shows a pair of images recorded at $\pm 22\,000$ Å defocus in attempt to make the distinction. The average ratio of amplitudes for strong reflections at about $1/40$ Å^{-1} was -0.92 before and -1.03 after correction for radiation damage. This ratio is close to the calculated ratio of -0.98 for 7% amplitude contrast, assuming it is a cosine term, but not to the calculated ratio of -0.87, assuming it is a constant term. Thus it would appear that the amplitude contrast is indeed a cosine term, substantiating the findings above that the specimen behaves as a "weak-phase–weak-amplitude" object.

3.4. Effect of ice thickness

A limited number of image pairs were recorded from tubes embedded in ice considerably thicker than, for example, in fig. 4. Estimates based on electron scattering calculations (ref. [15], see Methods) suggested that the thickness in these cases was at least 1,000 Å, compared to about 500 Å for the specimens examined in detail above. Values for the amplitude contribution determined

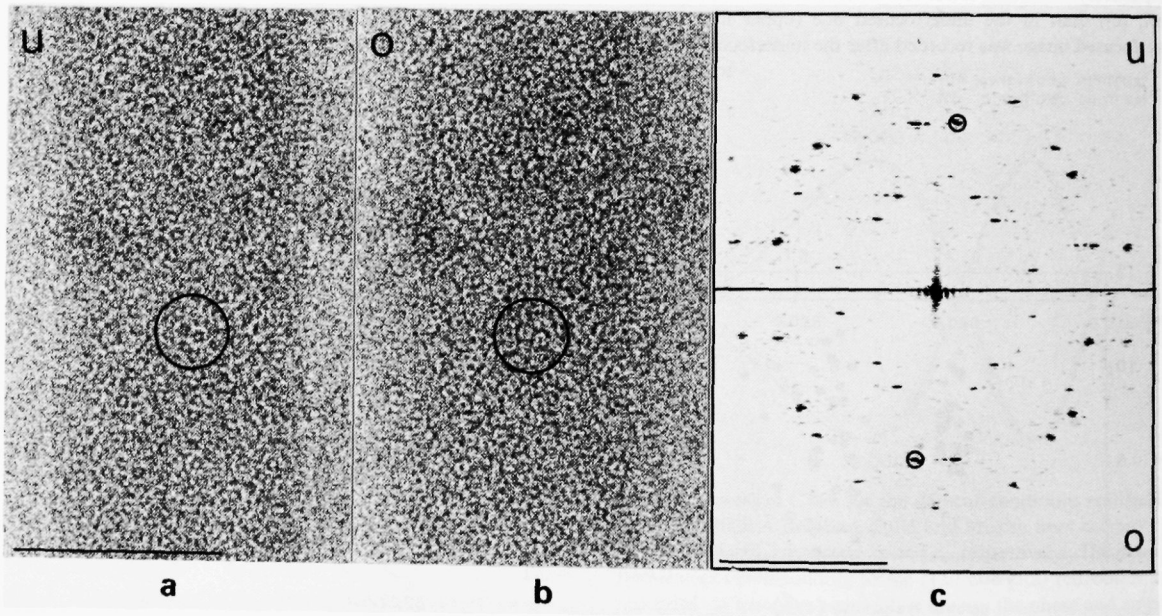

Fig. 10. Images of an ice-embedded tube recorded at 22000 Å underfocus (a) and subsequently at 22000 Å overfocus (b), and a composite of their diffraction patterns (c). The (1,2) reflections from one side of the tube are marked. U and O denote under- and overfocus, respectively. Note that the higher resolution reflections (e.g. (1,2)) appear very similar, whereas the lower resolution reflections appear slightly weaker in the transform from overfocused image (lower half, (c)); this should not happen if the amplitude contrast is a constant term (see fig. 9). The equivalence of the higher resolution reflections becomes clearer after correction for radiation damage (see text). Bars correspond to 0.1 μm (a) and $1/50$ Å^{-1} (c).

from the specimens embedded in thicker ice were also in the region of 7%.

4. Discussion

These experiments examined the contrast transfer for a typical thin biological specimen embedded in thin amorphous ice. A particular concern was to evaluate the amount and nature of the amplitude contrast contribution to the total contrast, and the method used was to compare information in the Fourier transforms of images recorded in pairs, at different defocuses. First, we determined (fig. 5) that the amplitude contrast contribution was independent of the periodicities in the specimen over the range 30-90 Å. Second, we determined that there was no influence of the magnitude of underfocus in the range 8,000-16,000 Å, which is typical of that used to optimally enhance the details of such specimens. Analysis of underfocus-overfocus pairs of images (for which the mean defocus is close to zero) confirmed the value determined for the amount of amplitude contrast in the above experiments (fig. 8). Third, we found that the amplitude contrast, consistent with the theory, was more appropriately described by a cosine term rather than by a constant term. The avérage value for the amplitude contrast contribution to the total contrast from the entire number of measurements (144) was 6.8% (SD = 2.8%), and all our findings were consistent with the linear theory, showing the specimen to behave as a "weak-phase–weak-amplitude" object.

It was also of interest to evaluate the dependence of the amplitude contrast on the thickness of the ice, since ice is a major source of inelastic scattering and may therefore be expected to play a role in influencing the contrast due to the coherent interaction of the electrons. A limited number of experiments, using ice thicknesses estimated to be at least two times greater than that needed to properly embed the specimen, gave the same results as for the thin ice. Hence there was no marked effect of ice thickness on the contrast modulation in the image over the range of spacings examined.

4.1. The method of defocus pairs for determining amplitude contrast

The method we applied to evaluate the amplitude contrast makes use of the fact that the amplitude of a given reflection in the Fourier transform of an image changes with defocus in a way that depends on the amount of amplitude contrast contributing to that image. This approach is more suitable than one involving a focal series (e.g., ref. [4]) for analysing frozen-hydrated specimens, because of their high susceptibility to radiation damage: it is impossible to record more than two or three successive images which give accurate information about the electron optical parameters and about the specimen at the same time. The accuracy of this method depends on the absolute values of the two defocuses used, their difference and the spacings in the specimen being considered. Too small a defocus renders the amplitudes of the reflections in the Fourier transform of the specimen difficult to measure, and too small a defocus difference will make the measurement unreliable unless very precise amplitudes can be obtained. For low resolution spacings, comparison of underfocused–overfocused pairs of images appears to provide the most accurate estimate for the amount of amplitude contrast, because the phase and amplitude contrast mechanisms reinforce each other in one case but tend to cancel in the other. It may also be possible to check the value derived quantitatively for the amplitude contrast by recording an image at the overfocus value where it is calculated that the contributions from phase and amplitude contrast should exactly cancel. However, in the case of the specimen studied here, cancellation of the lowest resolution principal reflection, the (1,0), would take place at a defocus of only ~ -4000 Å (given an amplitude contrast of 7%), which is too small to provide a good signal-to-noise ratio for most of the reflections.

It is of interest to note that for the particular specimen studied here the low resolution reflections were quite insensitive to radiation dose (fig. 3a). Thus it would be possible to record, successively, images at say 8000 Å underfocus and then 24000 Å underfocus to obtain information on all the relevant spacings, without their degradation

and at a good signal-to-noise ratio. If the amplitudes of all the reflections are obtained out to the first zero in the CTF in both cases, then a fairly uniform resultant CTF would be obtained simply by adding the two sets of data.

4.2. Relation to other work

The contrast transfer for frozen-hydrated specimens has not been evaluated previously by quantitative methods, and several alternative approaches have been used to compensate for over-enhancement of the high spatial frequencies due to defocusing. These include the use of X-ray intensities to provide appropriate values for the unmodulated amplitudes of the diffraction peaks [20]; compensation, or partial compensation of the CTF, assuming the specimen to be a pure phase object [21–23]; combination of several images of the same specimen recorded over a range of underfocus values [20,24]. None of these methods is entirely satisfactory. X-ray scattering factors have a different atomic number dependence from electron scattering factors, and X-ray diffraction patterns rarely relate directly to the Fourier transforms of electron images. Compensation of the CTF assuming phase contrast only is not accurate and may lead to undesirable amplification of the noise. Combining images of the same specimen entails scaling errors, which are compounded by the effect of radiation damage. Electron diffraction may yield figures for the unmodulated amplitudes of the diffraction peaks, but its use is generally restricted to large, well ordered arrays of molecules.

However, any of these approaches – and even uncompensated images – may be of value in highlighting certain features of the specimen, such as the subunit organization. Another highlighting effect of different origin may be achieved when negative staining is used, by partial penetration of the stain into the structure. The present analysis provides a more rational basis for making the compensation and, given that the effect of noise can be properly treated, provides the means for obtaining a more accurate representation of the densities composing the specimen.

An earlier analysis of the contrast transfer, based on a focal series of micrographs from negatively stained catalase crystals [4], yielded a value of 35% for the contribution due to amplitude contrast, as compared to the value of 7% obtained in this study. The difference is to be expected, at least in qualitative terms, because of the greater attenuation of the coherent incident wave by the heavy metal atoms. Second-order effects, e.g. multiple scattering, were barely detectable in the negative stain study, where the specimen thickness was ~ 200 Å; therefore it is reasonable that they were not detected in the present study, where the specimen thickness was ~ 300 Å and the individual diffracting layers were of half this thickness. A rough estimate assuming appropriate values for the mean inner potentials [25] suggests that the thickness limit for the validity of the linear approximation, applied to frozen-hydrated specimens, may be about four times that of the stained specimen, i.e. substantially thicker than investigated here.

Still to be explored experimentally is the contrast transfer at very low resolution, where inelastic scattering may play a more significant role, and at higher resolution, where it may have a smaller effect. Over the range of spatial frequencies we have examined the relative contributions to the total contrast made by the phase and amplitude terms ($A(\upsilon)$ and $B(\upsilon)$) were, within experimental error, constant. Over the wider range of spatial frequencies this is unlikely to be the case and in compensating for the CTF to derive a more accurate representation, it would be appropriate to synthesize separate "amplitude" and "phase" maps of the structure.

5. Conclusion

The contrast transfer for a typical (~ 300 Å thick) frozen-hydrated specimen was evaluated by comparing pairs of images recorded at different defocuses. The dependence of the contrast transfer function on the level of defocus and periodicities present in the specimen was that expected from a "weak-phase–weak-amplitude" object. The con-

tribution to the image contrast from amplitude contrast was 7%.

Acknowledgements

This research was supported by an NIH Grant (GM27764). C.T. is a postdoctoral fellow of the Muscular Dystrophy Association. Thanks are due to R. Glaeser and D. Misell for constructive and helpful comments.

References

[1] R.M. Glaeser, Ann. Rev. Phys. Chem. 36 (1985) 243.
[2] K.-J. Hanszen and B. Morgenstern, Z. Angew. Physik 19 (1965) 215.
[3] W. Hoppe, Acta Cryst. A26 (1970) 414.
[4] H.P. Erickson and A. Klug, Phil. Trans. Roy. Soc. London B26 (1971) 105.
[5] K.A. Taylor and R.M. Glaeser, J. Ultrastruct. Res. 55 (1976) 448.
[6] M. Adrian, J. Dubochet, J. Lepault and A.W. McDowall, Nature 308 (1984) 32.
[7] R.A. Milligan, A. Brisson and P.N.T. Unwin, Ultramicroscopy 13 (1984) 1.
[8] M. Stewart and G. Vigers, Nature 319 (1986) 631.
[9] P.N.T. Unwin and R. Henderson, J. Mol. Biol. 94 (1975) 425.
[10] A. Brisson and P.N.T. Unwin, J. Cell Biol. 99 (1984) 1202.
[11] A. Brisson and P.N.T. Unwin, Nature 315 (1985) 474.
[12] E. Kubalek, S. Ralston, J. Lindstrom and N. Unwin, J. Cell Biol. 105 (1987) 183.
[13] L.A. Amos, R. Henderson and P.N.T. Unwin, Progr. Biophys. Mol. Biol. 39 (1982) 183.
[14] R. Henderson, J.M. Baldwin, K.H. Downing, J. Lepault and F. Zemlin, Ultramicroscopy 19 (1986) 147.
[15] R. Eusemann, H. Rose and J. Dubochet, J. Microscopy (1982) 239.
[16] J.M. Cowley, Diffraction Physics, 2nd ed. (North-Holland, Amsterdam, 1981).
[17] J. Frank, Biophys. J. 12 (1972) 484.
[18] J.C.H. Spence, Experimental High Resolution Electron Microscopy (Clarendon, Oxford, 1981).
[19] F. Thon, Z. Naturforsch, 21a (1966) 476.
[20] S.D. Fuller, Cell 48 (1987) 923.
[21] J. Lepault and T. Pitt, EMBO J. 3 (1984) 101.
[22] J. Lepault and K. Leonard, J. Mol. Biol. 182 (1985) 431.
[23] E.-M. Mandelkow and E. Mandelkow, J. Mol. Biol. 181 (1985) 123.
[24] R.H. Vogel, S.W. Provencher, C.-H. von Bonsdorff, M. Adrian and J. Dubochet, Nature 320 (1986) 533.
[25] D.L. Misell, J. Phys. D (Appl. Phys.) 9 (1976) 1849.